A Compact Fault Tolerant 2-D Anemometer

Andrea Ria, *Senior Member, IEEE*, Paolo Bruschi, and Massimo Piotto, *Member, IEEE*

***Abstract*—A compact anemometer capable of detecting both the magnitude and the direction of the wind in 2-D is presented. The device relies on a recently formalized principle, consisting in combining the differential pressures measured across distinct diameters of a cylinder exposed to the wind to estimate the wind velocity and the incidence angle. The cylinder includes an ad hoc microfluidic structure with three sections of diametric pressure probes connected in parallel. The multisection approach has been adopted in order to increase the reliability of the device. The prototype has been fabricated with stereolithographic printing, while commercial differential pressure sensors with low power consumption are used to read the pressures. The results of detailed experiments performed in a wind tunnel in the range 4–30 m/s are reported. A maximum angular error of 6° and a speed relative error less than 5.3% have been obtained.**

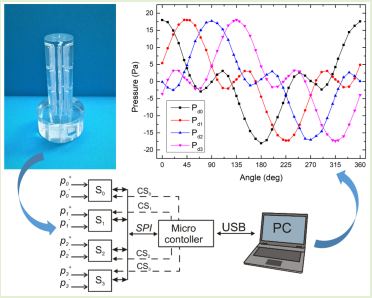

***Index Terms*—2-D anemometer, differential pressure anemometer, directional wind sensor, Internet of Things (IoT), sensor miniaturization, stereolithographic printing.**

I. Introduction

HISTORICALLY, anemometers have been used in different scenarios, such as meteorological studies, weather forecasting marine, and aerial navigation. With the advent of the Internet of Things (IoT) era, new fields of applications, such as the assistance in climate change studies, the spreading of pollutants, and the precise application of agrochemicals in smart agriculture [1] or the indoor climate control for well-being [2], are being proposed. In these emerging applications, one of the most promising approaches is the implementation of a wireless sensor network (WSN) with a large number of battery supplied nodes distributed on a wide area. In these cases, the availability of miniaturized and low power sensing devices is of primary importance.

The detection of wind speed and/or direction can rely on different principles of transduction. The simplest and most popular technique exploits a set of rotating cups to measure the wind speed and vanes to detect the direction. This kind of anemometer has low power consumption, but its miniaturization is very challenging. When mechanical devices are scaled down to centimeters scale, the frictional force tends to dominate over the inertial force due to the different scaling rules and this prevents a smooth movement at low speeds [3]. As a result, miniaturized mechanical anemometers based on rotating parts are not suitable for low wind speed applications.

A valid alternative is the ultrasonic anemometers. These devices are based on the time-of-flight principle and can be designed to detect two components of the wind velocity vector (2-D anemometers) or even all three components (3-D anemometers) [4]. However, the spacing among the ultrasonic transducers cannot be minimized without worsening the device sensitivity, thus limiting the downscaling of the anemometer [5].

Thermal anemometers are considered an effective substitute of cups and vane wind sensors when the detection of very slow air flows is required. They consist of one or more heated elements exposed to the wind and the quantity related to the wind speed is the gross heat loss or the heat transfer toward downwind direction [6], [7]. Miniaturization can be easily accomplished due to micromachining technologies [8], [9], [10], but the heating elements become extremely fragile and purpose-built packages are necessary.

Pressure probes represent another popular solution. The well-known Pitot tube is used in a wide range of applications to measure the magnitude of fluid flow velocity. Multihole pressure probes are proposed to detect both the direction and the speed of the wind by processing different values of pressure captured at the outer surface of a bluff or streamlined body exposed to the wind. For example, the commonly called "Cobra-probes" are capable of measuring the three components of fluid velocity at high frequency and they are very

Manuscript received 13 October 2023; revised 19 December 2023; accepted 12 January 2024. Date of publication 24 January 2024; date of current version 14 March 2024. This work was supported in part by ELSEL s.r.l (Italy) and in part by the Italian Ministry of Education and Research (MUR) in the Framework of the FoReLab and CrossLab Projects (Departments of Excellence). The associate editor coordinating the review of this article and approving it for publication was Prof. Meribout Mahmoud. *(Corresponding author: Massimo Piotto.)*

The authors are with the Department of Information Engineering, University of Pisa, 56126 Pisa, Italy (e-mail: andrea.ria@unipi.it; paolo.bruschi@unipi.it; massimo.piotto@unipi.i).

Digital Object Identifier 10.1109/JSEN.2024.3355500

compact [11]. However, conventional five-hole or seven-hole probes have a limited range of acceptance angles, usually less than 80° [12], [13]. Higher values of the acceptance angles have been obtained by increasing the number of the holes [14] at the price of more complex calibration procedures [15], [16]. The sampling of the pressure distribution on the surface of cylinders and spheres by means of a set of pressure-sensing holes has been proposed to extend the direction detection range to a 360° range [17], [18], [19], [20], [21], [22] and to obtain omnidirectional 3-D anemometers [23], [24]. A common method to estimate the wind speed and direction from the pressure measurements is based on empirical formulas derived from the fitting of the pressure distribution on the cylinder or sphere surface [17], [18], [19], [20], [21], [23], [24]. This method can be applied only to a restricted set of wind directions around the stagnation point since the pressure distribution is not monotonic. Usually, only pressures sampled up to 45° from the stagnation point can be used in the empirical formulas to obtain a good estimation of the wind direction. For this reason, the proposed transducing method requires first identifying the hole where the maximum of the pressure has been measured and then applying the empirical formulas to the pressures measured in this hole and in the adjacent ones. To extend the wind direction detection to the whole 360° range preserving a good resolution, a great number of holes is necessary. For example, Sun et al. [20] proposed a cylindrical probe with 12 pressure-sensing holes for a 2-D measurement, while spheres with 12 [24] and 30 pressure-sensing holes [23] are used to obtain an omnidirectional 3-D anemometer. Considering that each pressure-sensing hole is usually connected to an absolute pressure transducer, the complete devices turn out to be complex and quite large and this makes them unsuitable for noninvasive WSN applications. More compact devices have been obtained by connecting two holes placed at the ends of a diameter to the inputs of a differential pressure sensor [19], [21]. However, the transduction method does not change, and its processing complexity is not suitable for resource-restricted scenarios like the individual node of a large WSN or devices on board small autonomous vehicles. Recently, neural networks, processing several samples taken on the surface of a sphere, have been used to extract the wind direction and speed overcoming the complexity of the pressure distribution [22]. Such promising approach requires high computational power, which is currently not compatible with many low-cost, microcontroller-based embedded systems.

In 2009, we proposed a 2-D cylindrical anemometer [25] based on a novel transduction mechanism founded on a rigorous theory exposed in [26]. The proposed method exploits the symmetries of the pressure distribution on a cylinder surface with respect to the stagnation point. In the case of an ideal cylinder of infinite length, the symmetry property is independent of the wind speed, so the method is theoretically suitable for all flow regimes. The proposed algorithm is very simple and consists in linear algebraic operations applied to pressures sampled at specific positions on the cylinder surface. Performing the algebraic operations with a microfluidic network in the fluidic domain allows reducing both the number of external signal transducers and the complexity of the algorithms needed to estimate the quantities of interest. In fact, we obtained very compact and simple directional anemometers with the microfluidic network fabricated inside the cylinder by means of a computer-controlled milling machine [25], [27] or 3-D printing [28]. The devices used only two MEMS flow sensors operating as differential pressure transducers. However, these devices have also some drawbacks. In particular, the need for a laminar flow inside the microfluidic network makes it challenging to adapt these anemometers to high wind speed applications. Furthermore, the need of precise ratios between the hydraulic conductances of the microchannels that form the microfluidic network makes the sensors prone to partial or full obstructions of one or more channels caused, for example, by dust or dirt in outdoor applications or fabrication irregularities [26]. In addition, each channel fabricated inside the cylinder must have exactly the dimensions set in the design in order to avoid deviations from the predicted ideal behavior [28].

In this work, we propose a directional anemometer with a new configuration designed to overcome the mentioned drawbacks. In particular, we have implemented a transduction mechanism, where algebraic combinations of the pressures are performed by an electronic computer instead of a microfluidic network. In this way, deviations from the ideal behavior are minimized even at high wind velocities, and the proper functioning of the device is not compromised by partial obstructions of the microchannels or manufacturing dimensional errors. These improvements have been obtained at only the price of increasing the number of the external pressure transducers from two to four. In addition, to make the sensor more tolerant of even total obstructions of one or more channels, we have designed a redundant configuration consisting of three sets of pressure-sensing holes placed in the cylinder surface at different heights. A similar redundant solution has been proposed in previous works concerning different pressure probing schemes and processing [20]. Differently from [20], in the current work, we investigate the effects of blocking single and multiple holes, showing the actual effectiveness of the proposed configuration in counteracting this kind of impairment.

In Section II, we explain the theoretical principle of operation, whereas Section III describes the structure of the anemometer and introduces the adopted pressure sensors. In Section IV, we discuss the experimental results.

II. Principle of Operation

The proposed solid-state anemometer is capable of measuring both the direction and speed of the wind in 2-D. The principle of operation relies on the processing of the pressure distribution on the external surface of a cylinder exposed to an air stream. A thorough theoretical analysis is given in [26] and only a brief description is reported here.

When a fluid flows past a stationary body, like a cylinder, a region of disturbed flow is formed. The extent and the characteristics of the disturbed flow region depend on many factors, including the shape, orientation, and size of the body and the velocity and viscosity of the fluid. In the case of an idealized situation where disturbances like surface roughness,

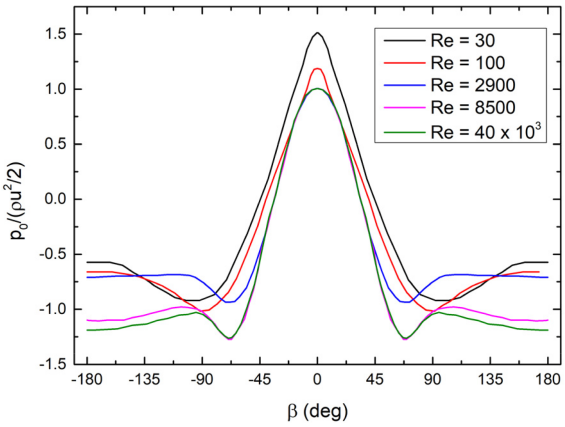

Fig. 1. Profile of normalized pressure p_0 around the cylinder surface for different Reynolds numbers (Re).

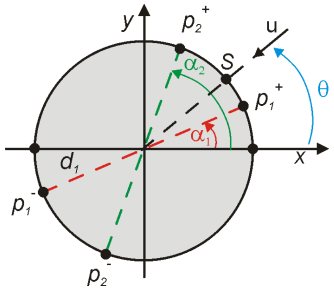

Fig. 2. Cylinder cross section showing the convention used for the quantities of interest. The wind velocity vector and its angle with x-axis are indicated with "**u**" and "θ," respectively.

wall proximity, and body end effects are neglected, the characteristics of the disturbed flow region are governed by a single parameter, namely the Reynolds number, defined as

$$\mathrm{Re} = \frac{\rho u D}{\mu} \tag{1}$$

where ρ is the air density, u is the wind speed, D is the cylinder diameter, and μ is the air viscosity.

The observed variations of the local velocity field around the cylinder are associated with a characteristic pressure distribution around its circumference. Fig. 1 shows the pressure distribution around the cylinder surface for different Reynolds number as a function of the angular distance β from the stagnation point, indicated with "S" in Fig. 2. The data have been obtained by precisely digitizing a set of experimental curves reported in [29] and, as a customary, the pressure values are normalized to the dynamic pressure ($\rho u^2/2$).

In [26], we first demonstrated that a differential pressure with a sinusoidal dependence on the wind direction can be obtained by linearly combining different diametric pressures, that is differential pressures developed by the wind across distinct diameters of the cylinder. Fig. 2 shows a cross section of a cylinder exposed to an air stream, whose velocity vector **u** forms an angle θ with the reference axis x. The diametric pressure P_d taken across a diameter forming an angle α with the x-axis is defined by

$$P_d(\alpha, \theta, u) = p^+(\alpha, \theta, u) - p^-(\alpha, \theta, u). \tag{2}$$

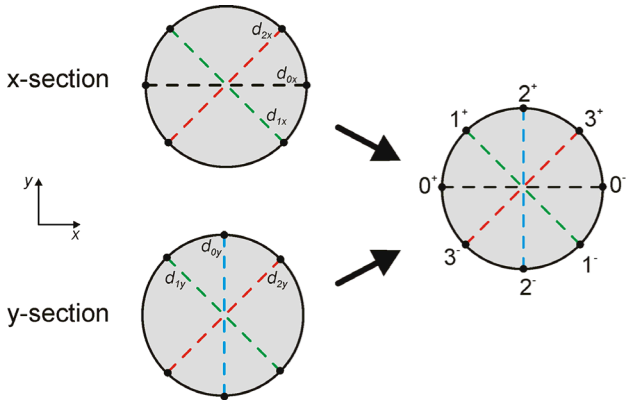

Fig. 3. Schematic view of the two orthogonal sets of diameters needed to obtain signals with cosine (x-section) and sine (y-section) dependence on the wind direction (left). Cross section of the proposed device with the merging of the x- and y-section (right).

In order to reduce the number of variables, it is convenient to define the diametric pressure for $\alpha = 0$ (i.e., the pressure across the diameter aligned with the x-axis) as

$$P_{d0}(\theta, u) = P_d(0, \theta, u). \tag{3}$$

It can be easily demonstrated that the differential pressure developed by the wind across a diameter forming an angle α_i with the x-axis can be expressed as

$$P_d(\alpha_i, \theta, u) = P_{d0}(\theta - \alpha_i, u) = P_{\mathrm{di}}(\theta, u). \tag{4}$$

It is worth noting that the single diametric pressure is still not monotonic and only the linear combination of a proper set of diametric pressures has a sinusoidal dependence on the wind direction [26].

Using two orthogonal identical sets of diameters, two signals with sine and cosine dependence on the wind direction, respectively, can be obtained, making estimation of the direction straightforward. The diametric pressures are sampled by means of pressure-sensing holes placed on the cylinder surface and connected to pressure sensors by means of an internal microfluidic network, as it will be described in Section III. Although the combination of a large number of diametric pressures produces a better approximation of the sinusoidal dependence, even a simple structure with three diameters was proven to give excellent results [26].

In this work, we have chosen to use the minimal configuration with the three diameters spaced of 45° each other, as schematically shown in Fig. 3 for the two set of diameters, namely, x- and y-section, necessary to obtain the cosine and sine signals. It can be noted that, using the 45° spacing, the two orthogonal sets of diameters have two diameters in common. As a result, only four independent diametric pressures instead of six are needed to estimate the wind direction and the final device is more compact with the x- and y-section merged into one section with four pairs of diametric pressure-sensing holes.

According to (4), the expressions of the four diametric pressures P_{d0}, P_{d1}, P_{d2}, and P_{d3} of the diameters shown in

Fig. 3 are

$$\begin{cases} P_{d0}(\theta,u) = p_0^+ - p_0^- \\ P_{d1}(\theta,u) = p_1^+ - p_1^- = P_{d0}\left(\theta - \dfrac{\pi}{4}, u\right) \\ P_{d2}(\theta,u) = p_2^+ - p_2^- = P_{d0}\left(\theta - \dfrac{\pi}{2}, u\right) \\ P_{d3}(\theta,u) = p_3^+ - p_3^- = P_{d0}\left(\theta - \dfrac{3}{4}\pi, u\right). \end{cases} \tag{5}$$

Applying the theory developed in [26], the following linear combinations of the diametric pressures are calculated:

$$p_X(\theta,u) = P_{d0}(\theta,u) + P_{d1}(\theta,u)\cos\left(\frac{\pi}{4}\right) - P_{d3}(\theta,u)\cos\left(\frac{\pi}{4}\right) \tag{6}$$

$$p_Y(\theta,u) = P_{d2}(\theta,u) + P_{d1}(\theta,u)\cos\left(\frac{\pi}{4}\right) + P_{d3}(\theta,u)\cos\left(\frac{\pi}{4}\right). \tag{7}$$

It has been demonstrated that the following approximations are valid:

$$p_X(\theta,u) \cong H(u)\cos(\theta) \tag{8}$$

$$p_Y(\theta,u) \cong H(u)\sin(\theta) \tag{9}$$

where $H(u)$ is a monotonic function of the wind speed.

Considering (8) and (9), the estimates of angle θ and magnitude H can be calculated by means of the following formula:

$$\begin{cases} \theta = \arctan(p_Y, p_X) \\ H(u) = \sqrt{p_X^2 + p_Y^2} \end{cases} \tag{10}$$

where "arctan" is the four-quadrant inverse tangent function. The wind velocity u can then be derived from H, since its dependence on the wind velocity is monotonic, as it will be shown later.

III. Description of the Prototype

A. Anemometer Description

Fig. 4 shows a schematic view of the horizontal and vertical cross sections of the designed cylinder.

The cylinder is 6 cm high with a diameter of 2 cm. The pressure developed by the wind on the cylinder outer surface is probed by microchannels that end on the surface at properly positioned holes. These pressure-sensing holes are grouped in sections, which are formed by holes placed at the same height from the cylinder base. In the proposed prototype, there are three sections, each one identified by its own height. Each section includes eight holes, forming 4 diameters, as described in Section II. The three sections, indicated with upper (Us), medium (Ms), and lower (Ls), are simply displaced from each other along the cylinder axis; therefore, holes and diameters are aligned.

Holes placed in different sections but at the same angular coordinate are connected together through longitudinal channels that end up at the cylinder base, where they are connected to differential pressure sensors, as schematically shown in Fig. 4.

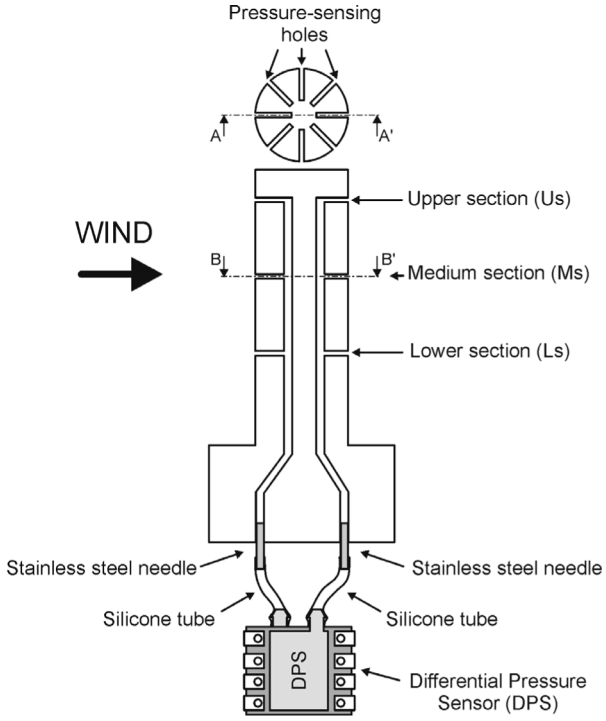

Fig. 4. Horizontal and vertical cross sections of the cylinder; the internal microfluidic network connecting the pressure-sensing holes to the differential pressure sensor is visible.

Since holes are placed at eight different angles, there are eight longitudinal channels, each one connected to three holes belonging to three different sections. Since it is necessary to probe the four diametric pressures, differential pressure sensors are connected between pairs of longitudinal channels that are connected to hole groups placed at opposite ends of diameters. As a result, four differential pressure sensors are required. External connection to the longitudinal channel was accomplished by inserting stainless steel needles into the holes in the bottom face of the cylinder, as schematically shown in Fig. 4. The needles were secured to the cylinder by means of epoxy resin, carefully deposited around the perimeter of the junction between the needles and the cylinder. Connections to the input ports of the differential pressure sensors were accomplished with silicone tubes.

Due to the microfluidic configuration shown in Fig. 4, each side of a diametric pressure relies on three different holes, reducing the probability of a total obstruction. Furthermore, only holes that, ideally, are placed at the same pressure are connected together; thus, the flow into the microchannels should be virtually zero, making the measured pressure independent on the hydraulic conductance of the channels.

The proposed prototype has been designed with the open-source software FreeCAD and fabricated by means of a stereolithography process with UTR-8100 resin available at PCBWay, Shenzhen, PRC [30]. This resin has a heat distortion temperature of +50 °C. Moreover, water absorption is less than 0.5%, which is lower than products used in previous work [25], [27], [28]. These properties improve the mechanical strength of the structure, making the anemometer more suitable for outdoor applications.

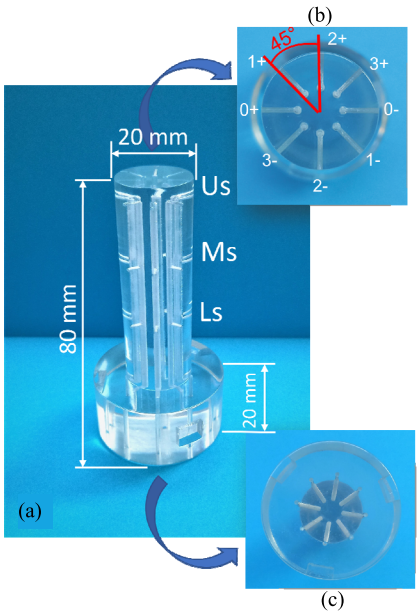

Fig. 5. (a) Photograph of the proposed anemometer with the main dimensions indicated. (b) Top and (c) bottom view of the anemometer.

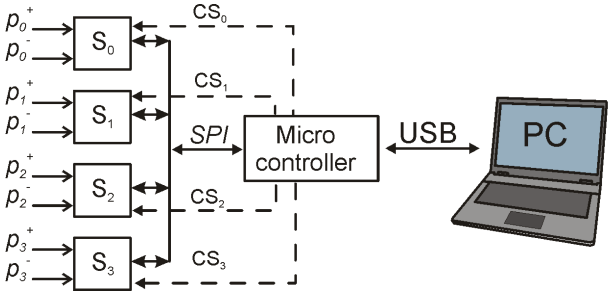

Fig. 6. Schematic view of the electronic interface; $S_{0\text{-}3}$ are the four differential pressure sensors, while the $CS_{0\text{-}3}$ are the CS_i lines.

Fig. 5 shows a photograph of the prototype with the main dimensions specified. The value of the diameter was chosen to allow the fabrication of the microfluidic network inside the cylinder without the risk of channel blockage due to the resolution limits of the 3-D printing process. In principle, the diameter could be reduced selecting a fabrication technique with a higher resolution. The cylinder has a 4 cm wide and 2 cm thick base to be correctly housed in the rotating stage used to characterize the device.

B. Differential Pressure Sensors

The choice of the differential pressure sensors was made taking into account different features, including pressure range, accuracy, total error band, compensated temperature range, and power consumption. From the experimental data in the literature concerning the pressure on the cylinder surface [29], it is found that, for a given wind velocity u, the maximum differential pressure is about equal to $P_{d\,\max} \simeq \rho u^2$. Considering the operating temperature range from −20 °C to +50 °C and a maximum wind speed of 30 m/s, a $P_{d\,\max}$ close to 1 kPa is expected. The RSC series of the piezoresistive silicon pressure sensor by Honeywell has been selected because it offers digital output (standard SPI interface) with adequate features in terms of resolution, accuracy, and power consumption. In particular, the selected differential pressure sensor (model: RSCMRRE001KDSE3) has the following properties: 1) ±1-kPa full-scale range; 2) total error band as low as ±0.25% full-scale span (FSS); 3) accuracy of ±0.1% FSS best fit straight line (BFSL); and 4) compensated temperature range from −40 °C to 85 °C. Furthermore, this family of sensors with a supply voltage of 3.3 V has a power consumption less than 6 mW in active mode, making them suitable for battery-supplied systems.

IV. Measurements Results and Discussion

A. Measurement Setup

The prototype was tested by means of a wind tunnel with a speed range from 4 to 30 m/s equipped with a reference Pitot probe. A rotating stage, equipped with a goniometer, hosts the anemometer in order to set the incidence angle.

Fig. 6 shows the schematic view of the electronic interface for data acquisition and processing. A custom printed circuit board (PCB) based on a microcontroller unit (MCU) MSP430i2041 by Texas Instruments was used to control the four differential pressure sensors (S_{0-3}) and perform data acquisition and preprocessing. Connection between the MCU and the sensors was via the SPI interface with four independent chip-select (CS_i) lines. The PCB includes an FTDI 231 USB-to-serial adapter to connect the MCU to a personal computer with a USB cable. The data processed by the MCU were then gathered by means of a Phyton-based software.

B. Experimental Results

In order to test the acquisition setup, the four differential pressures P_{di} were measured as a function of time with the wind speed set at 10 m/s and the incidence angle at 0°; 100 samples with a sampling rate of 10 Hz were acquired and the data are shown in Fig. 7, where the mean and the standard deviation of each signal are indicated. It can be noted that oscillations are present in all four curves due to the fluctuations of the air flow inside the wind tunnel. Applying the transduction algorithm to these data leads to the estimates of the wind direction and speed affected by fluctuations with a standard deviation of $\sigma_{\text{angle}} = 0.7°$ and $\sigma_{\text{speed}} = 0.07$ m/s, respectively. To mitigate the effects of the oscillations, the average of ten samples acquired with a sampling rate of 10 Hz was used as pressure sample in the device characterization.

A first set of measurements was performed with the device in the nominal condition, in which all three sections of the anemometer (Us, Ms, and Ls) are working without any obstruction of the pressure-sensing holes.

Fig. 8 shows the four differential pressures P_{di} as a function of the angle. The wind speed was set at 4.3 m/s and the incidence angle was varied by means of a rotating stage turned with an angular step of 10° with the addition of the angles 45°, 135°, 225°, and 315°.

The four differential pressures P_{di} show the same behavior with only angular shifts of multiple of 45°. It is worth noting that the pressure distributions reach the same maximum (minimum) values, confirming that the behavior of the four pressure sensors is sufficiently matched and that the fabrication

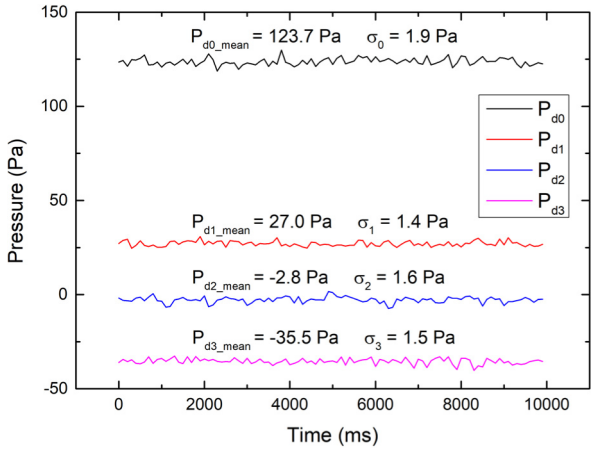

Fig. 7. Differential pressures as a function of time; the wind speed was set at 10 m/s, while the incidence angle was set at zero degrees; data were acquired with a sampling rate of 10 Hz; the mean value and the standard deviation of the data are indicated.

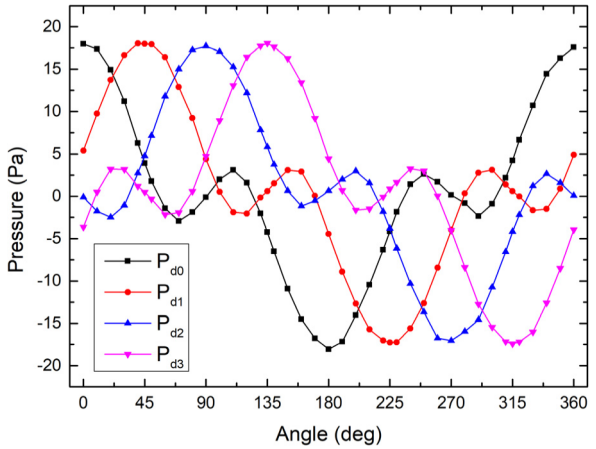

Fig. 8. Differential pressures as a function of the incidence angle; the wind speed was set at 4.3 m/s; each pressure value is the average of ten samples acquired with a sampling rate of 10 Hz.

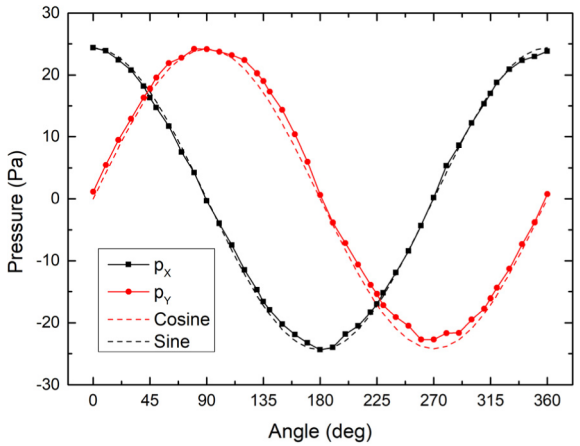

Fig. 9. Pressures p_X and p_Y with the wind speed set at 4.3 m/s. Ideal cosine and sine functions are added to facilitate the comparison.

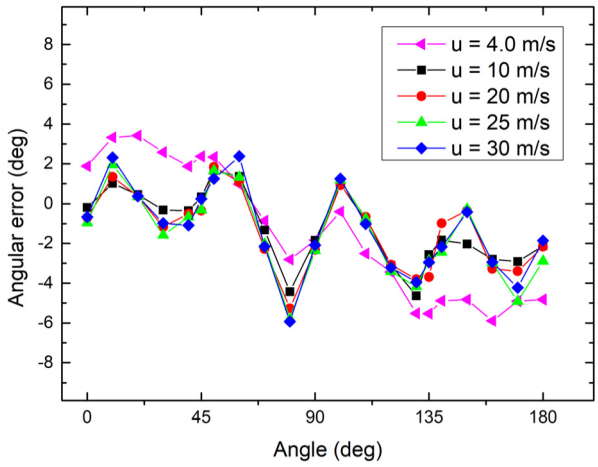

Fig. 10. Angular error as a function of the incidence angle for different values of the wind speed.

process was able to guarantee a good alignment between the three sections.

The two signals p_X and p_Y were calculated by means of (6) and (7) and the result is shown in Fig. 9, where the ideal cosine and sine functions have been added to facilitate comparison. It is possible to observe a good agreement between the experimental curves and the ideal functions. This provides an experimental proof of the theory presented in [26] and further confirms that the fabrication of the device is sufficiently accurate.

The device has been characterized with wind speeds from 4 to 30 m/s, varying the incidence angle in the 0°–180° interval with the same steps used for the data of Fig. 8. The incidence angle was estimated from the measured p_X and p_Y pairs applying a simple four-quadrant arctangent function. The resulting angular errors are shown in Fig. 10. From the experimental data of Fig. 10, it is possible to estimate an error interval of $[-6°, +4°]$ in the whole range of wind velocities examined. The error interval is significantly larger than the $[-2°, +2°]$ estimate in [26]. Furthermore, the curves show a decrease as the angle increases and a critical point at 80°, where the error is maximum for all the velocities greater than 4 m/s. These phenomena are not present in the theoretical error curves obtained in [26]. The possible explanations of these discrepancies can be: 1) finite length of the cylinder, with additional turbulence at the top and base of the cylinder; 2) nonnegligible size of the pressure probes (holes); and 3) nonuniform wind velocity in the wind tunnel. Nevertheless, a maximum error of 6° over such a wide velocity range can still be considered an acceptable result and it is consistent with the error values reported for similar devices in outdoor applications [21]. It is worth noting that this result has been obtained without applying complex fitting and postprocessing algorithms.

The wind speed measured by the proposed sensor is estimated from the quantity $H(u)$, which is calculated from p_X and p_Y using (10). From [26], $H(u)$ should be nearly independent of the incidence angle and be nearly equal to the maximum diametric pressure (ρu^2). However, when the wind direction is swept across the 180° interval, $H(u)$ shows oscillations due to the imperfect cosine approximation obtained with the proposed method. To filter out the effects of the oscillations, we have averaged the estimated $H(u)$ values across the 180° wind direction range for each wind speed, and the results are shown in Fig. 11. The curve suggests that the following general power law dependence can be used to fit the

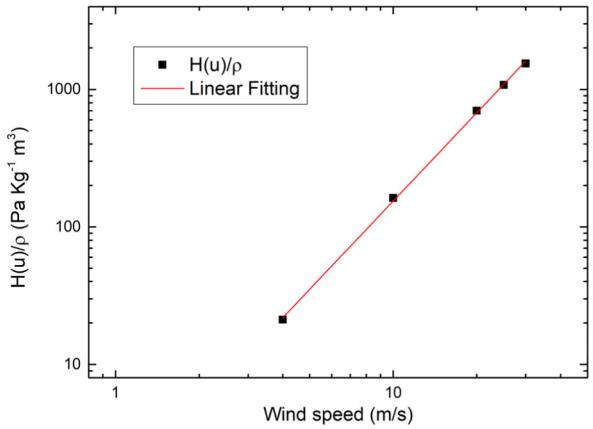

Fig. 11. Graph of the normalized $H(u)$ as a function of the wind speed (points) and the linear fit (solid line) in log–log coordinates.

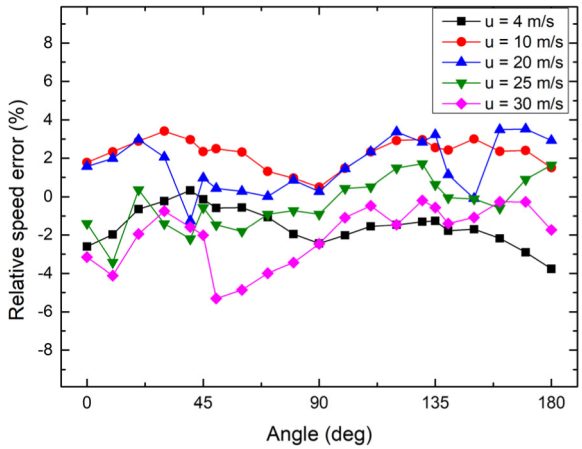

Fig. 12. Relative speed error as a function of the incidence angle for different values of the wind speed.

TABLE I
COMPARISON OF DIFFERENT DIRECTIONAL CYLINDRICAL ANEMOMETERS BASED ON PRESSURE MEASUREMENTS

Reference	Speed Range (m/s)	Maximum Angular Error	Maximum Relative Speed Error
Liu et al. [19]	2-40	5°	5 %
Pan et al. [21]	1-40	5°	5 %
Sun et al. [20]	5-60	4°	4 %
This work	4-30	6°	5.3%

data:

$$H(u) = a \cdot \rho \cdot u^b. \tag{11}$$

An optimum fit, shown in Fig. 11 by the solid line, can be obtained with $a = 1.136$ and $b = 2.133$. Note that the exponent b differs from the ideal value ($b = 2$) by only 7% while a variation of about 14% is obtained for the coefficient a (ideal value $a = 1$).

Inverting (11) with the mentioned values for coefficients a and b, we could estimate the wind velocity for any incidence angle and wind magnitude. Since $H(u)$ shows a residual dependence on the incidence angle [25], [26], we estimated the velocity error due to this nonideality. The results, shown in Fig. 12, demonstrate that the relative error is smaller than 4% for most of the conditions with a maximum value of 5.3% at 30 m/s.

TABLE II
ANGULAR ERROR FOR THE FIRST FAULT TOLERANT TEST

Sections	Maximum Angular Error at 4.3 m/s	Maximum Relative Speed Error at 4.3 m/s
Us	3.1°	5.6 %
Ms	3.0°	4.4 %
Ls	4.9°	11.3 %

In Table I, the calculated angular and speed errors are compared to the values of other cylindrical anemometers operating in a similar wind speed range. The obtained angular and speed errors turn out to be similar or slightly higher than the state-of-the-art devices, which adopt fitting of the real experimental curves to extract the measurands [19], [21], or an empirical approximation of the pressure distribution requiring a high number of pressure sensors [20]. In the proposed approach, the angle is calculated using simple expressions derived from the theory [26], while the velocity determination relies on an elementary two-parameters power law. In this respect, the obtained accuracy can be considered a good starting point for further improvements. It is worth mentioning that the upper and lower limits of the velocity range investigated in this work are due to a limitation of the wind tunnel used to carry out the experimental tests. Different from previous works present in [19], [20], and [21], the proposed approach is not based on the approximations of specific experimental curves but exploits the symmetry properties of the pressure distribution being, in principle, applicable to extremely wide velocity ranges. In practice, the main factor limiting the velocity range is the operating range of the pressure sensors. Considering that the maximum differential pressure is about equal to $P_{d\,\max} \simeq \rho u^2$, the peak value for wind velocity of 1 m/s is in the order of 1 Pa; thus, pressure sensors with resolution well below 1 Pa are required to enable operation at low wind velocities. On the other hand, in order to employ the proposed anemometer for speeds higher than 30 m/s, it would be necessary to select differential pressure sensors with a higher measurement range.

C. Fault Tolerance Tests

In order to evaluate the tolerance of the proposed device when some holes are obstructed, we performed two different kinds of failure test.

In the first one, we emulated the condition in which only one section still works, while the holes of the other two sections are all closed. The results are shown in Fig. 13, where the p_X and p_Y pressures measured with a single section are compared with the nominal case, where all sections are available (ALL). The wind speed was set to 4.3 m/s.

The pressures p_X and p_Y of each section do not reach the same maximum (minimum) values. This may be related to the fact that the pressure distributions shown in Fig. 1 are referred to a cylinder of infinite height, i.e., a cylinder, where the turbulence effects created by the free end and the base can be neglected. In a cylinder of finite height, the distribution of the surface pressure along the vertical axis is not constant [31].

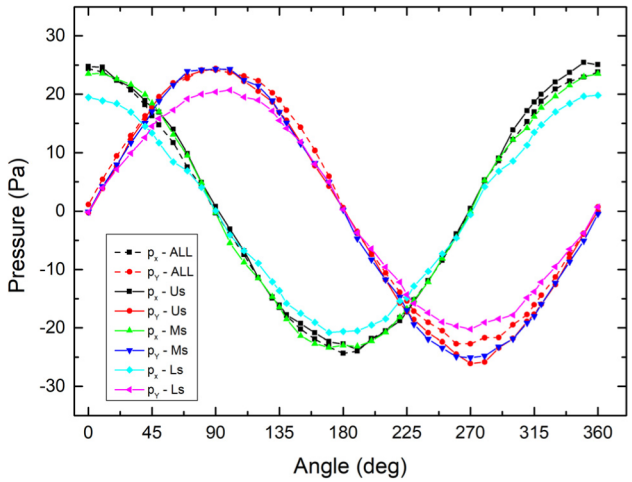

Fig. 13. Pressures p_X and p_Y measured using four different configurations: nominal condition with all sections working (ALL); three fault conditions with only the upper section (Us), or the medium section (Ms) or the lower section (Ls) working. The wind speed was set at 4.3 m/s.

TABLE III
SECOND FAILURE TEST SENSING HOLES SETUP

Sections	Pressure-sensing holes							
	0^+	0^-	1^+	1^-	2^+	2^-	3^+	3^-
Us	C	C	C	O	O	C	C	O
Ms	O	C	C	C	C	C	O	C
Ls	C	O	O	C	C	O	C	C

O=OPEN, C=CLOSED

The maximum angular error was calculated for each section at 4.3 m/s and the results are shown in Table II. It can be observed that the worst case angular error is less than 5°, showing that the device continues to work properly even with all the holes of two sections completely closed. The maximum angular error when a singular section operates is slightly better than the value shown in Fig. 10 for the device working at 4 m/s in the ideal nominal condition. Further investigation is required to explain this phenomenon, which is reasonably related to the way averaging of the pressures of different sections occurs in the hydraulic domain. The relative speed error of the Us and Ms sections is comparable to that measured with the device in the ideal nominal condition. The Ls section shows a clear worsening in the wind velocity detection. This behavior may be due to the turbulence created by the cylinder base.

In the second test, we verified the behavior of the device in a more random situation, where some holes belonging to different sections are closed. We have considered the limit case, where the four diametric pressures P_{di} are measured by means of only eight open holes placed in different sections. Table III resumes the configuration of the anemometer for this test: for each section, a channel has been left open (O) or closed (C). In this configuration, and each diametric pressure is available even if obtained with holes belonging to different sections. For better understanding, the pressure P_{d0}, for example, is obtained as the difference between p_0^+ of the Ms section and the p_0^- of the Ls section. Similar choices are made for the other diametrical pressures. The test was performed with the wind speed set to 4.3 m/s.

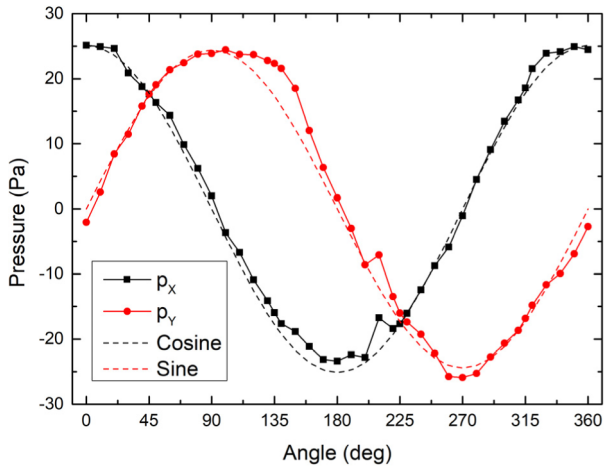

Fig. 14. Pressures p_X and p_Y measured with the sensing holes configured as reported in Table III. The wind speed was set at 4.3 m/s. The ideal cosine and sine functions are added to facilitate the comparison.

Fig. 14 shows p_X and p_Y compared to the ideal cosine and sine functions. Clearly, in this case, the behavior gets worse, but the proposed measurement method allows obtaining two signals that are quite similar to a sine and a cosine curve for many angle values. Applying (10), we have estimated the wind direction with a maximum angular error of 14.5° and the wind velocity with a maximum relative speed error of 12.5%. These values confirm that the device can be still useful even in this extreme working condition for applications where rough wind speed and direction estimations are required.

Finally, the effects of the inclination of the cylinder axis with respect to the wind velocity vector have been investigated. The device has been mounted on a tilting stage placed in front of the outlet of a wind tunnel. The cylinder has been tested with all sections operating, and the angle β, formed by the cylinder axis with the flow direction, was varied form 0° (no inclination) to 30°. The experiments were performed at a wind speed of 4 m/s. Similar to [28], we found a nearly uniform attenuation of the differential pressures by a $\cos(\beta)$ factor. As a result, no significant increase of the angular error was detected, while the device inclination resulted in underestimating the wind speed.

V. CONCLUSION

In this article, a fault tolerant, compact directional anemometer has been proposed. The transduction method consists in simple processing of four diametric pressures sampled by means of small holes on the surface of a compact cylinder. Angular error less than 6° and speed relative error less than 5.3% have been obtained in the range 4–30 m/s. The compactness of the structure, the low power consumption of the pressure transducers, and the simplicity of the algorithms make the proposed device suitable for IoT applications. Furthermore, a redundant hole configuration has been designed in order to make the device tolerant to the total obstruction of a large number of pressure-sensing holes. This property allows the extension of the device applications to outdoor or harsh environments.

ACKNOWLEDGMENT

The authors wish to thank ELSEL s.r.l. (Italy) for providing the wind tunnel for the experimental characterization of the devices.

REFERENCES

[1] V. K. Quy et al., "IoT-enabled smart agriculture: Architecture, applications, and challenges," *Appl. Sci.*, vol. 12, no. 7, p. 3396, Mar. 2022, doi: 10.3390/app12073396.

[2] E. Arens et al., "Measuring 3D indoor air velocity via an inexpensive low-power ultrasonic anemometer," *Energy Buildings*, vol. 211, Mar. 2020, Art. no. 109805, doi: 10.1016/j.enbuild.2020.109805.

[3] Z. Rymuza, "Control tribological and mechanical properties of MEMS surfaces. Part 1: Critical review," *Microsyst. Technol.*, vol. 5, no. 4, pp. 173–180, Jul. 1999.

[4] E. Boni, L. Pugi, M. Montagni, and A. S. Savoia, "High performance vector ultrasound anemometer based on capacitive micromachined ultrasonic transducers," in *Proc. IEEE Int. Ultrason. Symp. (IUS)*, Oct. 2019, pp. 1594–1596, doi: 10.1109/ULTSYM.2019.8925718.

[5] J. C. Wyngaard and S.-F. Zhang, "Transducer-shadow effects on turbulence spectra measured by sonic anemometers," *J. Atmos. Ocean. Technol.*, vol. 2, no. 4, pp. 548–558, Dec. 1985.

[6] L. M. Fingerson, "Thermal anemometry, current state, and future directions," *Rev. Scientific Instrum.*, vol. 65, no. 2, pp. 285–300, Feb. 1994.

[7] N.-T. Nguyen, "A novel thermal sensor concept for flow direction and flow velocity," *IEEE Sensors J.*, vol. 5, no. 6, pp. 1224–1234, Dec. 2005.

[8] F. Mayer, A. Haberli, H. Jacobs, G. Ofner, O. Paul, and H. Baltes, "Single-chip CMOS anemometer," in *IEDM Tech. Dig.*, Washington, DC, USA, 1997, pp. 895–898.

[9] Y. Zhu, B. Chen, M. Qin, and Q.-A. Huang, "2-D micromachined thermal wind sensors—A review," *IEEE Internet Things J.*, vol. 1, no. 3, pp. 216–232, Jun. 2014.

[10] H.-B. Liu, N. Lin, S.-S. Pan, J. Miao, and L. K. Norford, "High sensitivity, miniature, full 2-D anemometer based on MEMS hot-film sensors," *IEEE Sensors J.*, vol. 13, no. 5, pp. 1914–1920, May 2013, doi: 10.1109/JSEN.2012.2236014.

[11] J. Chen, B. S. Haynes, and D. F. Fletcher, "Cobra probe measurements of mean velocities, Reynolds stresses and higher-order velocity correlations in pipe flow," *Experim. Thermal Fluid Sci.*, vol. 21, no. 4, pp. 206–217, May 2000.

[12] *Aeroprobe, Multi-Hole Probes*. Accessed: Sep. 2023. [Online]. Available: https://www.aeroprobe.com/cobra-probe/

[13] T. Yao, S.-D. Zhou, M. Wang, S. Ye, and Y.-C. Zhang, "Optimal design of hemispherical 7-Hole probe tip with perpendicular holes," *IEEE Access*, vol. 9, pp. 85101–85108, 2021.

[14] H. Wang, X. Chen, and W. Zhao, "Development of a 17-hole omnidirectional pressure probe," *AIAA J.*, vol. 50, no. 6, pp. 1426–1430, Jun. 2012.

[15] S. Shaw-Ward, A. Titchmarsh, and D. M. Birch, "Calibration and use of n-Hole velocity probes," *AIAA J.*, vol. 53, no. 2, pp. 336–346, Feb. 2015.

[16] A. Ghosh, D. M. Birch, and O. Marxen, "Neural-network-based sensor data fusion for multi-hole fluid velocity probes," *IEEE Sensors J.*, vol. 20, no. 10, pp. 5398–5405, May 2020.

[17] J. L. Amick and G. C. Gill, "A stationary cylindrical wind speed and direction sensor for use in model testing," in *Proc. Int. Res. Seminar Wind Effects Buildings Struct.*, Ottawa, ONT, Canada, Sep. 1967, pp. 1–23.

[18] D. Surry, A. McDougall, and I. Murley, "A miniature cylindrical wind speed and direction sensor," *J. Wind Eng. Ind. Aerodynamics*, vol. 38, nos. 2–3, pp. 469–481, Jul. 1991.

[19] C. Liu, L. Du, and Z. Zhao, "A directional cylindrical anemometer with four sets of differential pressure sensors," *Rev. Sci. Instrum.*, vol. 87, no. 3, Mar. 2016, Art. no. 035105.

[20] B. Sun, W. Zhou, M.-Z. Yuan, E.-Q. Fang, and N. Gan, "A cylindrical vehicle-mounted anemometer based on 12 pressure sensors—Principle, prototype design, and validation," *IEEE Sensors J.*, vol. 18, no. 17, pp. 6954–6961, Sep. 2018.

[21] Y. Pan et al., "High accuracy and miniature 2-D wind sensor for boundary layer meteorological observation," *Sensors*, vol. 19, no. 5, p. 1194, Mar. 2019.

[22] K. Haneda, K. Matsudaira, and H. Takahashi, "Neural network-based airflow vector sensor using multiple MEMS differential pressure sensors," *IEEE Access*, vol. 11, pp. 40978–40987, 2023.

[23] R. M. Eckman, R. J. Dobosy, D. L. Auble, T. W. Strong, and T. L. Crawford, "A pressure-sphere anemometer for measuring turbulence and fluxes in hurricanes," *J. Atmos. Ocean. Technol.*, vol. 24, no. 6, pp. 994–1007, Jun. 2007.

[24] V. Ramakrishnan and O. K. Rediniotis, "Development of a 12-hole omnidirectional flow-velocity measurement probe," *AIAA J.*, vol. 45, no. 6, pp. 1430–1432, Jun. 2007.

[25] P. Bruschi, M. Dei, and M. Piotto, "A low-power 2-D wind sensor based on integrated flow meters," *IEEE Sensors J.*, vol. 9, no. 12, pp. 1688–1696, Dec. 2009, doi: 10.1109/JSEN.2009.2030652.

[26] P. Bruschi and M. Piotto, "Determination of the wind speed and direction by means of fluidic-domain signal processing," *IEEE Sensors J.*, vol. 18, no. 3, pp. 985–994, Feb. 2018, doi: 10.1109/JSEN.2017.2780521.

[27] P. Bruschi, A. Ria, and M. Piotto, "A scalable 2D, low power airflow probe for unmanned vehicle and WSN applications," in *Applications in Electronics Pervading Industry, Environment and Society* (Lecture Notes in Electrical Engineering), vol. 573, S. Saponara and A. De Gloria, Eds. Cham, Switzerland: Springer, 2019, doi: 10.1007/978-3-030-11973-7_12.

[28] A. Ria, A. Catania, P. Bruschi, and M. Piotto, "Experimental evaluation of a 3D-printed fluidic system for a directional anemometer," *Sensors*, vol. 20, no. 15, p. 4094, Jul. 2020, doi: 10.3390/s20154094.

[29] M. M. Zdravkovich, *Flow Around Circular Cylinders: A Comprehensive Guide Through Flow Phenomena, Experiments, Applications, Mathematical Models and Computer Simulations*, vol. 1. Oxford, U.K.: Oxford Univ. Press, 1997, pp. 1–109.

[30] *Pcbway, UTR-8100*. Accessed: Sep. 2023. [Online]. Available: https://www.pcbway.com/rapid-prototyping/3d-printing/plastic/resin/UTR-8100/

[31] T. Okamoto and M. Yagita, "The experimental investigation on the flow past a circular cylinder of finite length placed normal to the plane surface in a uniform stream," *Bull. JSME*, vol. 16, no. 95, pp. 805–814, 1973.

Andrea Ria (Senior Member, IEEE) received the bachelor's, master's, and Ph.D. degrees in electronics engineering from the University of Pisa, Pisa, Italy, in 2014, 2016, and 2021, respectively.

He is currently a Researcher with the Department of Information Engineering of University of Pisa. His research interests include low-voltage and low-power mixed-signal integrated sensor interfaces.

Dr. Ria won the "Distinguished Service Award" during the RFID-TA Conference in 2019. In 2018, he received the second prize of "Huawei Italy University Challenge." He is the Vice Chair of IEEE Student Branch of University of Pisa.

Paolo Bruschi received the Laurea degree in electronic engineering from the University of Pisa, Pisa, Italy, in 1989, and the Perfezionamento degree, equivalent to the Ph.D., from the Sant'Anna University School of Pisa, Pisa, in 1992.

In 1993, he joined with the Dipartimento di Ingegneria dell'Informazione, University of Pisa, where he is currently a Full Professor. His research interests are in the field of mixed signal integrated circuit, ultralow-voltage electronics, and MEMS sensors modeling and technology.

Massimo Piotto (Member, IEEE) received the Laurea degree in electronic engineering from the University of Pisa, Pisa, Italy, in 1996, and the Ph.D. degree in electronic, computer, and telecommunication engineering from the University of Pisa, in 2000.

From 2001 to 2017, he was a Researcher of the Italian National Research Council. Since 2018, he has been an Associate Professor with the Information Engineering Department, University of Pisa. His research interests include the design of integrated sensors and actuators, the development of MEMS, and the design of electronic circuits for sensor interfacing.

Open Access funding provided by 'Università di Pisa' within the CRUI-CARE Agreement